J Mater Sci: Mater Med (2009) 20:1839–1848
DOI 10.1007/s10856-009-3763-8

# The development of a scanning strategy for the manufacture of porous biomaterials by selective laser melting

**R. Stamp · P. Fox · W. O'Neill · E. Jones · C. Sutcliffe**

Received: 8 January 2009 / Accepted: 24 April 2009 / Published online: 18 June 2009


**Abstract** Porous structures are used in orthopaedics to promote biological fixation between metal implant and host bone. In order to achieve rapid and high volumes of bone ingrowth the structures must be manufactured from a biocompatible material and possess high interconnected porosities, pore sizes between 100 and 700 μm and mechanical strengths that withstand the anticipated biomechanical loads. The challenge is to develop a manufacturing process that can cost effectively produce structures that meet these requirements. The research presented in this paper describes the development of a 'beam overlap' technique for manufacturing porous structures in commercially pure titanium using the Selective Laser Melting (SLM) rapid manufacturing technique. A candidate bone ingrowth structure (71% porosity, 440 μm mean pore diameter and 70 MPa compression strength) was produced and used to manufacture a final shape orthopaedic component. These results suggest that SLM beam overlap is a promising technique for manufacturing final shape functional bone ingrowth materials.

R. Stamp (✉) · P. Fox · C. Sutcliffe
MSERC, Department of Engineering, University of Liverpool, Harrison Hughes Building, Brownlow Hill, Liverpool L69 3GH, UK
e-mail: rstamp@liverpool.ac.uk

W. O'Neill
University of Cambridge, Cambridge, UK

E. Jones
Stryker Orthopaedics, Limerick, Ireland

## 1 Introduction

The development of materials with controlled porosity has largely been driven by the requirements of the medical device industry. Typically, the controlled porosity materials are applied to devices that interface with human tissue for prolonged periods, for example Total Hip/Knee Replacements. In such devices the porous structure is either used as a coating on an underlying solid substrate providing a surface for bone in-growth [1] or as a structure that modifies the modulus of the device allowing the matching of the implant stiffness with that of the host bone [2]. A variety of methods for the manufacture of porous systems have been developed with the specific aim of creating a structure that provides properties suitable for the production of orthopaedic devices [3–7]. Methods such as sintered beads [4, 7], fibre mesh [3, 6] and thermal spray processes [5], whilst successful commercially, have several distinct disadvantages. For example in the application of sintered beads to a substrate implant microstructure (and hence mechanical and fatigue strength) is compromised [8, 9] and the optimum level of porosity is impossible to attain [10], whilst the thermal spray processes do not produce structures with interconnecting porosity and optimum pore size [11].

More recently developed processes, for example Chemical Vapour Deposited (CVD) Foams [12] address these issues with reported success [13, 14] albeit with a complex, multistage process which is incapable of producing parts directly with minimal, further downstream operations.

Within the medical industry three metallic materials groups are commonly used in load bearing situations [15], titanium alloys, cobalt-chrome and stainless steel. Of these, commercially pure titanium (CpTi) is the most important

material for porous bio-structures as it possesses excellent corrosion resistance, is biocompatible, and has a high strength to weight ratio [16]. A potential disadvantage of using titanium is related to its high chemical reactivity, especially with interstitial elements such as oxygen, carbon, nitrogen and hydrogen [16]. For this reason, titanium is thermally processed under a protective atmosphere, containing low levels of oxygen [17] or under vacuum.

The challenge therefore is to develop a process for the manufacture of CpTi components, taking into account the aforementioned processing difficulties with the required pore size, porosity and interconnectivity.

The automatic generation of 3-D objects from CAD data has been possible for over a quarter of a century using the techniques of layered manufacturing more commonly referred to as Rapid Prototyping (RP) [18]. Amongst these methods are Selective Laser Sintering (SLS), Selective Laser Melting (SLM), Stereolithography (SL), Blown Powder Cladding (BPC) and 3D Printing (3DP). These RP techniques rely on the same basic premise. Firstly, a CAD file representing the component geometry is sliced into thin horizontal layers using a mathematical algorithm. Then, the data representing each slice layer is sent to an automatic machine where material is deposited in a layer-wise method and selectively processed to produce a representation of the slice data. Finally, these steps are repeated, each layer being stacked one on top of the other until the final geometry is realised. Typical methods for selective processing are by the thermal action of high-energy beams on powder (SLS or SLM) [19]; the action of lower energy beams on liquids causing photopolymerisation (SLA) [20]; the binding of powder materials with liquids from printing heads (3DP) [21]; and the thermal action of high-energy beams on a gas borne powder (BPC) [22].

The laser processing of biocompatible titanium powders to produce porous structures on solids has the benefit that the composition and macrostructure can be graded in a controlled manner [23]. Early work on this process was published by Abe et al. [24], who used an Nd:YAG laser to investigate the direct production of bio-structures from commercially pure titanium powders.

Hollander et al. [25] used selective laser melting SLM to fabricate porous structures from Ti6Al4V alloy. Cylindrical test pieces were produced with nominal pore size of 600–1000 μm but limited interconnectivity. Mechanical testing confirmed that the strength was similar to conventionally produced porous materials and that the structure was conducive to osteoblast attachment.

It is clear from the literature that RP processes have been used for the production of implants but such devices have generally been solid, non-structured and patient specific [26]. This preliminary study explores the notion of utilising this technology in a broader scope whereby it can be used as a stand-alone manufacturing process for the production of highly porous components which can be manufactured at the high rates and volumes required for off-the-shelf deployment in hospitals. The initial work presented is focused on structures that can be built either directly or indirectly on to existing surfaces. In this paper, the technique employed will be referred to as a "beam overlap" process using the SLM method.

The porous "beam overlap" structure will be assessed against the specification for porous orthopaedic materials given in Table 1.

**Table 1** Requirements for orthopaedic bone ingrowth structures

| Parameter | Specification | Reference source |
|---|---|---|
| Pore size | 100–700 μm | [11, 13, 27–29] |
| Porosity | >65% | [11, 13, 28, 30, 31] |
| Compression strength | >50 Mpa | [32–38] |
| Surface topography | Free of particulate debris | [39–41] |
| Visual appearance | Similar to the trabecular bone being replaced | In-house surgeon panel review (assessment technique not reported in this paper) |

## 2 Materials and methods

### 2.1 Materials

The powder used for this research is spherical CpTi grade 1 gas atomised powder with a particle size normally distributed between 0 and 45 μm (Sumitomo Japan).

### 2.2 Sample manufacture

The test samples (30 mm tall compression specimens of both square and circular section) were manufactured using an MCP Realizer II, a commercial SLM workstation with a 200 W continuous wave Ytterbium Fibre Laser operating at a wavelength of 1071 nm (manufacturers specification 1065–1105 nm). The system uses a dual axis optical scanner (Cambridge Technology, USA), which directs the laser beam in the $x$ and $y$ direction. A flat field is generated using a 300 mm focal length f-Theta lens (Sill, Germany) to produce a focussed beam spot size of variable spot size, with a minimum calculated Gaussian spot diameter of 54 μm. Since the powder is fully melted during the process, protection of the SLM-processed parts from oxidation is essential, therefore all metal powder processing occurs in an inert (Argon) atmosphere of 0.2% $O_2$ or less.

A schematic of the SLM process is shown in Fig. 1 in which a layer of powder is deposited on to a substrate plate

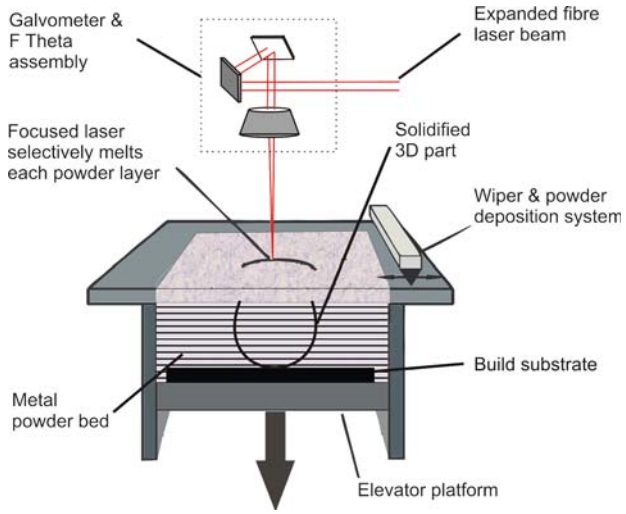


**Fig. 1** The SLM process as used in the MCP Realizer SLM systems

(seated on an elevator) and is spread uniformly by a wiper. The fibre laser fully melts the pre-deposited powder layer according to a specific computer-generated pattern. The melted particles fuse and solidify to form a layer of the component. The build platform then moves down a layer thickness of 50 μm and a new powder layer is spread and scanned. The process is repeated until all the layers have been melted, producing a physical representation of the original virtual 3D geometry. The substrate plate with attached manufactured parts is removed from the machine and the un-fused powder is collected, sieved and stored for reuse. Further processing steps required to complete the sample manufacture are EDM wire cutting to remove the parts for the plate, ultrasonic cleaning to remove residual un-fused powder, drying, labelling and storing.

### 2.3 Scanning strategies

The standard scanning strategy for the production of solid parts using SLM is described in Fig. 2. Scan contours are separated by a hatch spacing measured from the centreline of the current contour to that of the adjacent contour. A boundary contour surrounds the geometry to improve surface finish and in each subsequent layer the hatch lines are rotationally disposed to the previous layer by 90°. Contours are scanned by the laser by breaking the lines into a sequence of points and then actuating the laser on each point for a specified period of time.

The scanning strategy described above was modified for this study to allow for the production of porous parts. These parts were created by selecting the laser processing parameters to produce walls of the thickness, $d_{wt}$, and hatch spacing, $d_{hs}$, so that there was no overlap between the individual scan lines. In order to produce the desired pore depth, each layer was repeated a number of times until the desired wall height, $d_{hh}$, was obtained. No inner or outer boundaries were used in the beam overlap structure. This is represented in Fig. 3 with experimental settings being given in Table 2.

During processing a significant percentage of the first scanned layer of each hatch set is melted over free powder rather than previously melted solid. Scanning on free powder as opposed to previously melted solid has been shown to create an increased proportion of sintered rather than melted material [42]. Sintered powder volumes were minimised in the study by using exposure times that are 50% of those shown in Table 2 for the first layer of each set of hatches. The purpose of this is to form a discrete sintered powder layer that restricts thermal penetration into the powder bed and reduces this sintering effect.

Two 10 mm cube specimens for microscopic analysis, six vertical (Z) and six horizontal (Y) 30 mm long compression specimens were manufactured for each condition. Compression specimens built in the Z orientation had a 15 mm diameter circular section whilst those built in the Y orientation had a 15 mm square section in order to avoid a time consuming EDM wire cutting step. Clearly this difference in the sample geometry may cause variations in the

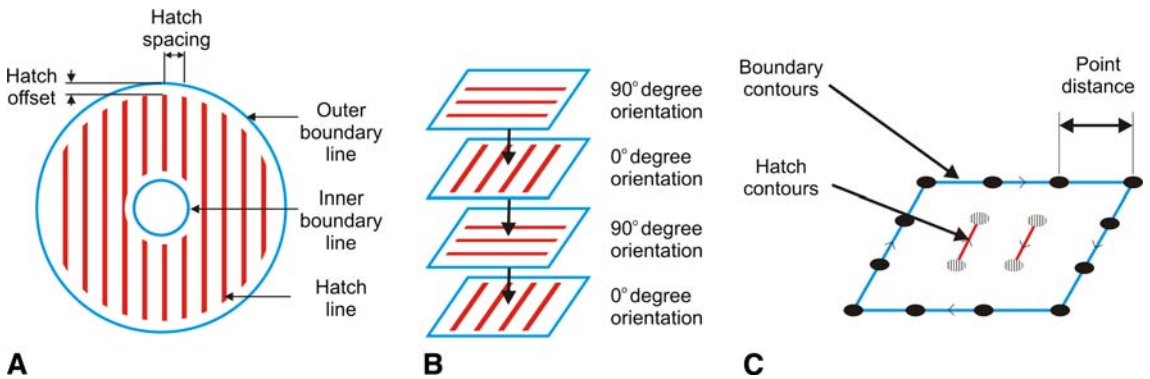


**Fig. 2** The SLM laser scanning strategy for melting layer geometries. **a** The boundary and hatch geometry types, **b** The 90° layer orientations that used to create solid geometries and **c** The melting strategy for solid contours

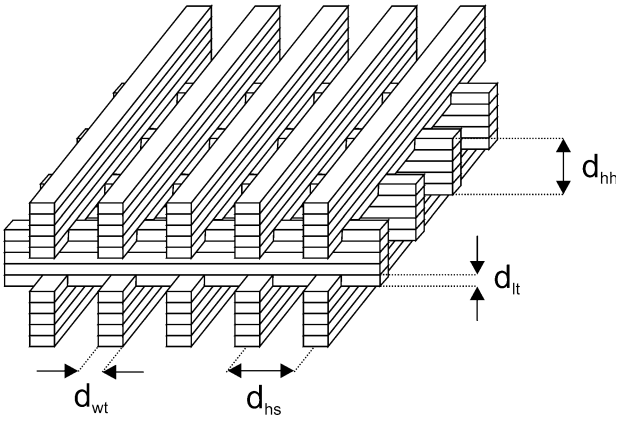


**Fig. 3** The design of the beam overlap porous structure

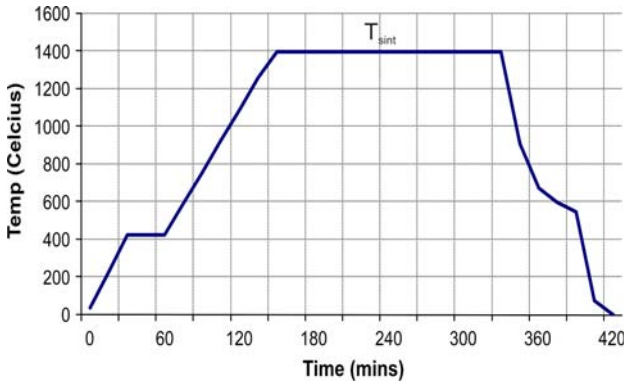


**Fig. 4** Sinter cycle profile used for treating beam overlap CpTi wafers

**Table 2** Experimental conditions for the beam overlap porous structures

| Specimen ID | $d_{hs}$ (μm) | $d_{hh}$ (μm) | Laser processing parameters |
|---|---|---|---|
| 1 | 700 | 750 | $d_{lt}$ = 50 μm |
| 2 | 800 | 850 | Laser power = 70 W |
| 3 | 900 | 950 | Point distance = 60 μm |
| | | | Point exposure time = 150 μs* |
| 4 | 700 | 750 | $d_{lt}$ = 50 μm |
| 5 | 800 | 850 | Laser power = 80 W |
| 6 | 900 | 950 | Point distance = 50 μm |
| | | | Point exposure time = 250 μs* |

* Point exposure times for the first layer of set of hatches are 50% of the values given

two sets of results. In order to clarify if this affected results, an experiment was conducted where five square and five cylindrical section compression samples were manufactured in the Z orientation using the structure and processing conditions described for condition 5. On compression testing no statistically significant difference was found between compression strengths of the two groups.

### 2.4 Post-manufacture heat treatment

Post-manufacture heat treatment was investigated using a high-vacuum sintering furnace (VSF HEQ 2624), operating at 5 Torr and back filled with Argon during cooling. The temperature/time profile for the sintering process is shown in Fig. 4. Half of specimens from each sample group were processed using this procedure.

### 2.5 Analysis equipment and techniques

A scanning electron microscope (Hitachi S-2460 N, Japan, acceleration voltage of 25 kV, 6 nm resolution 6 mm working distance) was used to assess surface topography and the presence of structural defects within the samples. Pore sizes were measured by analysis of the SEM images. Mean $d_{wt}$ and $d_{hh}$ values were calculated by drawing parallel lines which represent the surfaces of the walls as shown in Fig. 6. $D_{hh}$ is measured over a 3 mm section of a single wall and the $d_{wt}$ calculated by averaging the widths of three walls. The pore diameter is the maximum diameter of circle that is bounded by a pore. The pore dimensions in the XY plane ($PD_{top}X$ and $PD_{top}Y$) and YZ plane ($PD_{side}X$ and $PD_{side}Y$) were calculated using Eqs. 1–3. The percent open porosity is defined as the area of open pores per unit cross sectional area and was calculated for both the side and top view images.

$$PD_{top}X = PD_{top}Y = d_{hs} - d_{wt} \quad (1)$$

$$PD_{side}X = d_{hs} - d_{wt}. \quad (2)$$

$$PD_{side}Y = 2_{dhh(theoretical)} - d_{hh(measured)} \quad (3)$$

Porosity was determined gravimetrically using Eq. 4 from mean dimensional measurements taken using digital callipers (accuracy 0.002 cm). The specimen mass was measured using a top loading balance (AE ACB 600 H) to an accuracy of 0.01 g.

$$P = 1 - \frac{M/V}{\rho_{Ti}} \quad (4)$$

where $P$ is the porosity, $M$ the mass (g), $V$ the volume ($cm^3$), $\rho_{Ti}$ is the density of CpTi = 4.5 $g/cm^3$.

Compression testing was carried out in accordance with ASTM standard E9 [43] using a mechanical testing machine (Instron series 9) fitted with a 50KN load cell. A crosshead speed of 25.4 mm/min was used to 33% strain. Yield load was calculated using the cellular metal foam technique described by Gibson & Ashby [44], and was defined as the intersection of two gradients (the initial loading and the stress plateau), as shown in Fig. 5.

Metallographic analysis was performed on the 10 mm cubic specimens. These samples were polished using

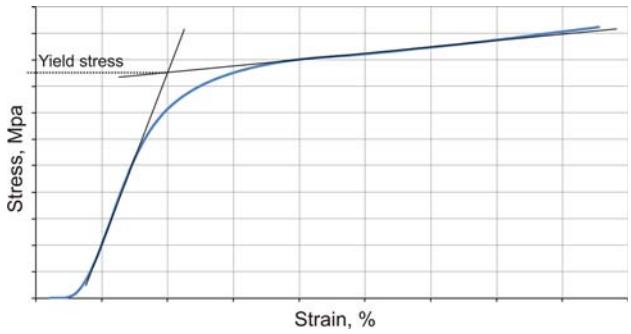


**Fig. 5** Typical stress strain curve for an SLM manufactured porous material

emery discs, diamond paste and colloidal silicate solution to a finish of better than 1 μm. Polished specimens were etched for 30 s with a solution of 100 ml $H_20$, 5 ml $NH_4FHF$ and 2 ml HCl for 30 s prior to being gold coated for SEM analysis.

Unless stated otherwise statistical significance was tested using student's *t* test using two tails and assuming equal variance. A confidence threshold of 95% was used to determine statistical significance.

## 3 Results

SEM photographs of vacuum sintered samples from each group are shown in Fig. 6. The samples have a regular, rectangular and interconnected pore distribution. The side and top images show that the distribution of pores is directionally dependent because the wall profiles create thick horizontal bars in the side view but not top view. This observation is reflected by the pore diameter and percentage open porosity measurements presented in Fig. 7. Whilst the specimens have equivalent pore diameters in side and top planes, the percentage of open pores in each sample group is increased by a mean 21.6% for the top compared with the side. The pore diameters increase with $D_{hs}$ as predicted by the theory and all specimens measured exhibit pore diameters between 400 and 800 μm. The mean wall widths, $d_{wt}$, and layer thickness, $d_{ht}$, are given in Table 3. The data shows that measured values of $d_{ht}$ are larger than the model values given in Table 2, and that this difference increases between the 70 and 80 W processing conditions. The wall thickness is also shown to vary between 213 and 269 μm and shows a statistically significant increase (Unsintered *P* value 0.004) from the 70 W to 80 W processing conditions.

In the higher magnification images in Fig. 8, a microtexture is evident on the surfaces of the walls. In the as-manufactured state this can be seen to be spherical metal powder particles which are sintered to the surface of the structure during manufacturing. High vacuum sintering causes these particles to remelt into the main body of the walls and individual particles are no longer discernable. The measured $d_{wt}$ and $d_{hh}$ data presented in Table 3 shows that mean $d_{hh}$ values increase for sintered compared to as

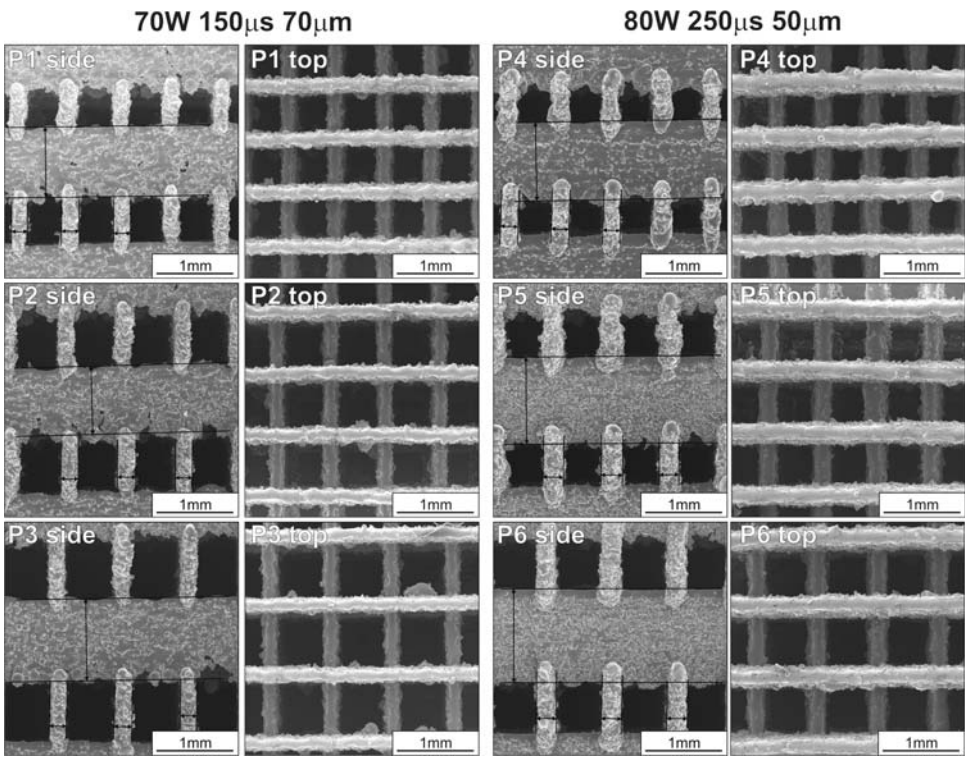


**Fig. 6** SEM photographs of the sintered specimens from each group in side and top view

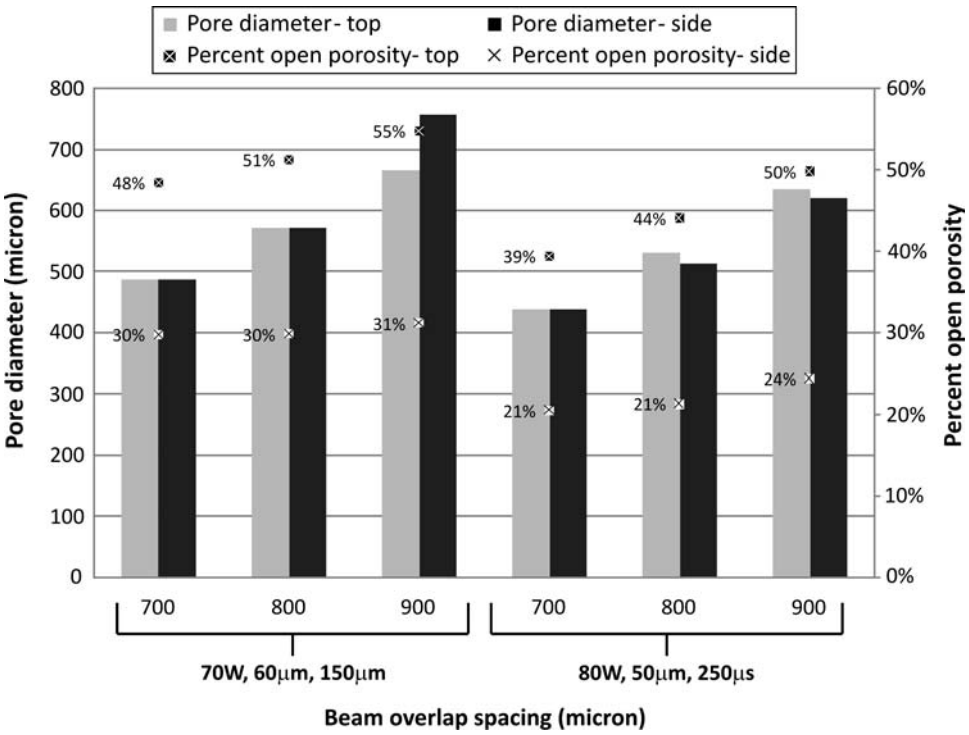


**Fig. 7** Pore diameter and percentage open porosity of the as-manufactured specimens as a function of beam overlap spacing, $d_{hs}$, and laser processing parameters

**Table 3** Measured wall width and height for each specimen group

| Specimen ID | $d_{wt}$ (micron) | | $d_{hh}$ measured – $d_{hh}$ modelled (micron) | |
|---|---|---|---|---|
| | As-manufactured | Sintered | As-manufactured | Sintered |
| 1 | 213 | 221 | 51 | 168 |
| 2 | 227 | 233 | 83 | 109 |
| 3 | 234 | 224 | 92 | 119 |
| 4 | 260 | 230 | 192 | 275 |
| 5 | 269 | 269 | 236 | 279 |
| 6 | 265 | 265 | 228 | 274 |

manufactured samples. There is no statistically significant change in the $d_{wt}$ values of the two groups.

Mechanical strength and porosity as a function of wall spacing is given in Fig. 9. There are two discrete sets of data shown on this bar chart. The data on the left hand side is obtained using low powers and exposures (Table 2) and the data on the right hand side is obtained from the high powers and exposures. The higher strengths obtained with the high powers and exposures are associated with better melting and thicker walls (metal flows at higher temperatures making walls thicker at the expense of porosity). The graph also shows the relationship between mechanical

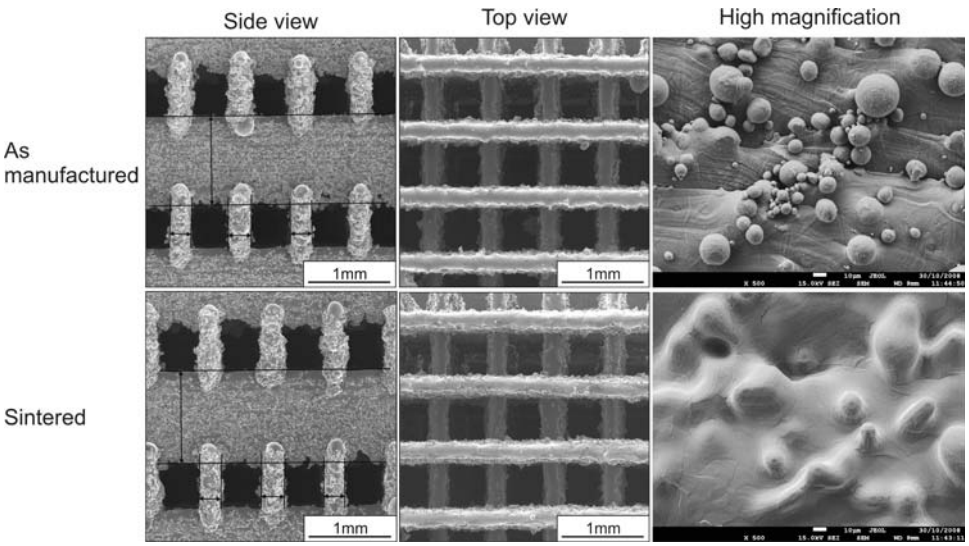


**Fig. 8** SEM photographs of an as-manufactured and vacuum sintered group 4 specimen

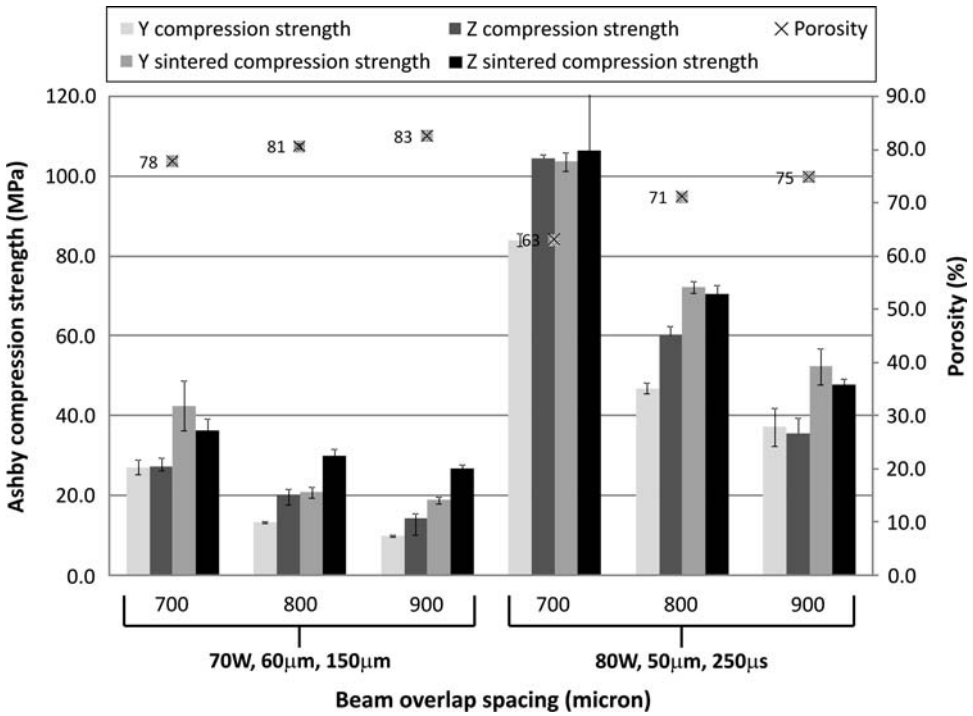


**Fig. 9** Porosity and compression strength pre- and post-sintering as a function of beam overlap spacing $d_{hs}$ and laser processing parameters

**Table 4** Impact of sintering on mechanical strength

| Specimen ID | Beam overlap spacing (μm) | Processing conditions | % Compression strength change with sintering | |
|---|---|---|---|---|
| | | | Y orientation | Z orientation |
| 1 | 700 | 70 W, 60 μm, 150 μs | 57 | 32 |
| 2 | 800 | | 56 | 48 |
| 3 | 900 | | 89 | 87 |
| 4 | 700 | 80 W, 50 μm, 250 μs | 42 | 10 |
| 5 | 800 | | 54 | 17 |
| 6 | 900 | | 41 | 34 |

strength and porosity. The variation in compression strength with sintering is shown in Fig. 9 and Table 4. Y and Z strengths are reported for each condition. Sintering is shown to increase the Y and Z compression strengths of all sample groups manufactured at both low and high laser powers.

Metallographic sections (side view) of the as-manufactured and sintered specimen 4 are shown in Fig. 10. The as-manufactured microstructure has a martensitic type appearance with small (50–100 μm) irregular grains without clear internal features. The sintered microstructure can be seen to have large (>500 μm) equiaxed grains.

## 4 Discussion

The beam overlap technique has been used to create porous CpTi structures of controlled and interconnected porosity. Structures have been developed with pore diameters in the range of 400–700 μm and volumetric porosities between 62 and 83%. Compression strength has been shown to have an inverse relationship to porosity and structures have been produced whose as-manufactured compression strengths vary between 10 and 104 Mpa.

The post manufacture sintering step has been shown to further increase the mechanical strengths for all sample groups and to modify the surface topography of the structures. The surface tension and creep behaviour induced by the high temperature vacuum sintering process causes the sintered powder particles that adhere to the surface of the walls to reabsorb into the walls, which produces a micro surface roughness. Micro surface roughness has been previously shown to promote osteo-integration [45], so it is possible that the rough surface topography of the sintered specimens would enhance its performance as a bone ingrowth structure.

The metallographic analysis in Fig. 10 shows the as-manufactured sample to have an $\alpha'$ lath martensitic type structure, which is typical of $\alpha$ titanium alloys rapidly

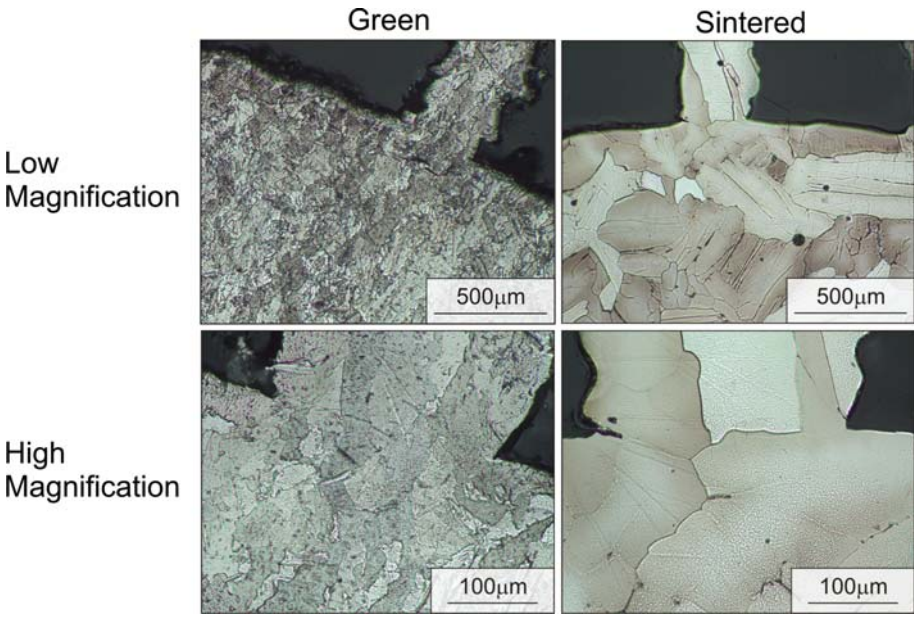


**Fig. 10** Micrographs of the as-manufactured and sintered specimen 4 (side view)

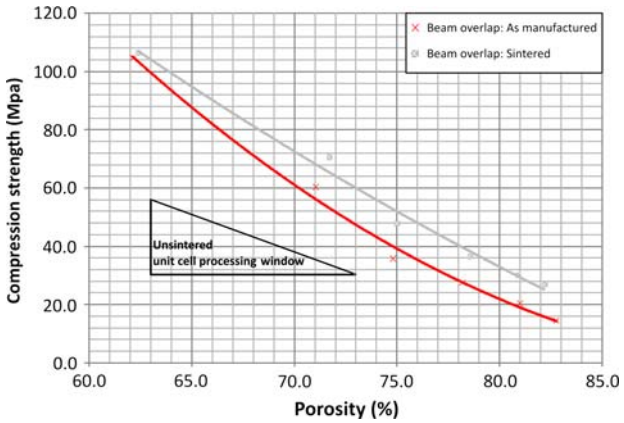


**Fig. 11** Strength/porosity relationship of beam overlap and unit cell CpTi SLM structures [46]

cooled from the $\beta$ phase. During the sintering process the CpTi is slowly cooled from the $\beta$ region and forms large grains with widmanstatten lamella.

Beam overlap structures have been shown to satisfy all the requirements for bone ingrowth structures listed in Table 1. A sintered beam overlap structure designed with the parameters described for specimen group five would produce a 71% porous structure with a mean pore diameter of 440 μm and compression strength above 70 MPa. The strength: porosity ratio of these structures compares favourably to the unit cell bone ingrowth SLM structures reported by Mullen et al. [46], as shown in Fig. 11. Both studies use <45 μm CpTi powder in MCP Realizer SLM systems. It is suggested that the increased strength for the beam overlap structures is derived from the use of parallel walls as opposed to the network of wire strands in the unit cell approach.

A potential negative of the beam overlap structures is that the pore distribution is directionally dependent. In the side view the walls are seen in profile, which decreases the line of sight porosity compared to the highly open top view. This contributes to the geometric pattern produced on

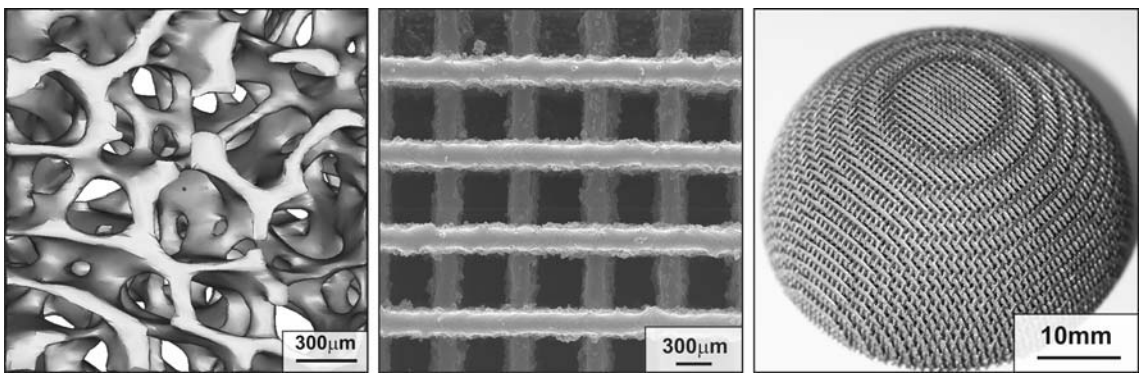


**Fig. 12** *Left*: CT scan image of trabecular bone structure. Centre: SEM image of beam overlap structure (condition 4). *Right*: A porous titanium hemisphere manufactured with $d_{ha}$ of 700 μm

the hemispherical sample in Fig. 12. The ordered pattern produced by the beam overlap structures contrasts with the random organic nature of trabecular bone that is being replaced. This may be considered a limitation of the technique since there is a commercial requirement that the bone ingrowth surfaces of orthopaedic component closely resemble the bone being replaced (source: internal surgeon review panel). Existing orthopaedic metal foams, such as the chemical vapour deposition (CVD) foam described by Bobyn et al. [12], better achieve this organic appearance. It would therefore be desirable to develop a technique for creating beam overlap structures with a less directional and more random appearance. Given the design freedom afforded by SLM manufacturing techniques, the authors consider this modification to be achievable for the beam overlap technique.

## 5 Conclusions

This paper has demonstrated the process of SLM for producing porous structures of controlled porosity by a beam overlap procedure. The important requirements for pore size, porosity and mechanical strength are easily attainable. It has been shown that it is possible to work at significantly higher porosities yet still meet the mechanical requirements. This may be an important consideration for devices that require higher porosities and strength, such as spinal implants. Post manufacture high vacuum sintering has been used to increase the compression strength and enhance the surface topography of the structures. The technique has been used to populate CAD volumes and create final shape orthopaedic components, as shown in Fig. 12. Further work is envisaged to overcome to directionality of the structure, which distorts the visual appearance particularly in planar structures. However this proposed manufacturing process shows definite merit for producing components that require interconnected porosity and pores of a particular size.

**Acknowledgements** The authors would like to thank the Engineering and Physical Sciences Research Council (EPSRC) and Stryker Orthopaedics for funding this research. Thanks also to L. Bailey for technical support.

## References

1. Mont MA, Hungerford DS. Proximally coated ingrowth prostheses. A review. Clin Orthop Relat Res. 1997;344:139–49.
2. Crowninshield RD, Brand RA, Pedersen DR. A stress analysis of acetabular reconstruction in protrusio acetabuli. J Bone Joint Surg. 1983;65:495–9.
3. Della Valle CJ, Berger RA, Shott S, Rosenberg AG, Jacobs JJ, Quigley L, et al. Primary total hip arthroplasty with a porous-coated acetabular component. A concise follow-up of a previous report. J Bone Joint Surg. 2004;86-A:1217–22.
4. Engh CA, Hopper RH Jr. The Odyssey of porous-coated fixation. J Arthroplasty. 2002;17:102–7. doi:10.1054/arth.2002.32547.
5. McCutchen JW, Collier JP, Mayor MB. Osseointegration of titanium implants in total hip arthroplasty. Clin Orthop Relat Res.. 1990;261:114–25.
6. Petersen MB, Poulsen IH, Thomsen J, Solgaard S. The hemispherical harris-galante acetabular cup, inserted without cement. The results of an eight to eleven-year follow-up of one hundred and sixty-eight hips. J Bone Joint Surg. 1999;81:219–24.
7. Rodriguez JA. Acetabular fixation options: notes from the other side. J Arthroplasty. 2006;21:93–6. doi:10.1016/j.arth.2006.02.152.
8. Georgette FS, Davidson JA. The effect of HIPing on the fatigue and tensile strength of a case, porous-coated Co-Cr-Mo alloy. J Biomed Mater Res. 2004;20:1229–48.
9. Manley MT, Kotzar G, Stern LS, Wilde A. Effects of repetitive loading on the integrity of porous coatings. Clin Orthop Relat Res. 1987;217:293–302.
10. Hamman G. In: Lemons JE, editor. Quantitative characterization and performance of porous implants for hard tissue applications ASTM STP 953. Philadelphia: ASTM; 1987. p. 77.
11. Bobyn JDPD, Pilliar RMPD, Cameron HUMD, Weatherly GCPD. The optimum pore size for the fixation of porous-surfaced metal implants by the ingrowth of bone. Clin Orthop Relat Res. 1980;150:263–70.
12. Bobyn J, Stackpool G, Toh K-K, Hacking S, Tanzer M, Krygier J. Bone ingrowth characteristics and interface mechanics of a new porous tantalum biomaterial. J Bone Joint Surg. 1999;81-B:907–14. doi:10.1302/0301-620X.81B5.9283.
13. Bobyn J, Toh K, Hacking S, Tanzer M, Krygier J. Tissue response to porous tantalum acetabular cups: a canine model. J Arthroplasty. 1999;13:347–54. doi:10.1016/S0883-5403(99)90062-1.
14. Gruen TA, Poggie RA, Lewallen DG, Hanssen AD, Lewis RJ, O'Keefe TJ, et al. Radiographic evaluation of a mono-block acetabular component. J Arthroplasty. 2005;20:369–78. doi:10.1016/j.arth.2004.12.049.
15. Ward LP, Strafford KN, Wilks TP, Subramanian C. The roll of refractory element based coating on the tribological and biological behavior of orthopaedic implants. J Mater Process Technol. 1996;56:364–74. doi:10.1016/0924-0136(95)01850-6.
16. Santos EC, Osakada K, Shiomi M, Kitamura Y, Abe F. Microstructure and mechanical properties of pure titanium models fabricated by selective laser melting. Proc Inst Mech Eng Part C J Mech Eng Sci. 2004;218:711–9.
17. Arcella FG, Abbott DH, House MA. Rapid laser forming of titanium structures. Grenada, Spain: Metallurgy World Conference; 1998.
18. Gerbhardt A. Rapid prototyping. Munich: Hanser publishers; 2003.
19. Householder R. Molding process, US, 1979.
20. Hopkinson N, Dickens PM. Emerging rapid manufacturing processes. In: Hopkinson N, Hague RJM, Dickens PM, editors. Rapid manufacturing: an industrial revolution for the digital age. USA: John Wiley & sons; 2006.
21. Chua CK, Leong KF, Lim CS. Powder-based rapid prototyping systems. In: Rapid prototyping: principles and applications. Singapore: World Scientific; 2003.
22. Keicher DM, Love JW, Dullea KJ, Bullen JL, Gorman PH, Smith ME. Forming structures from CAD solid models. US Patent; 2004.
23. Abbott DH, Arcella FG. Aeromet implementing novel Ti process. Met Powder Rep. 1998;53:24–6.
24. Abe F, Osakada K, Kitamura Y, Matsumoto M, Shiomi M. Manufacturing of titanium parts for medical purposes by selective laser melting. In: Rapid prototyping. Tokyo, Japan: University of Dayton; 2000. p. 288–293.

25. Hollander DA, von Walter M, Wirtz T, Sellei R, Schmidt-Rohlfing B, Paar O, et al. Structural, mechanical and in vitro characterization of individually structured Ti–6Al–4V produced by direct laser forming. Biomaterials. 2006;27:955–63. doi:10.1016/j.biomaterials.2005.07.041.
26. Sercombe T, Jones N, Day R, Kop A. Heat treatment of Ti-6Al-7Nb components produced by selective laser melting. Rapid Prototyping J. 2008;14:300–4. doi:10.1108/13552540810907974.
27. Hulbert SF, Klawitter JJ, Talbert CD, Fitts CT. Research in dental and medical materials. New York: Plenum; 1969. p. 19.
28. Nilles JL, Coletti JM, Wilson C. Biomechanical evaluation of bone porous material interfaces. J Biomed Mater Res. 1973;7:231–51. doi:10.1002/jbm.820070211.
29. Harris WH, Jasty M. Bone ingrowth into porous coated canine acetabular replacements: the effect of pore size, apposition, and dislocation. Hip. 1985;214–34.
30. Assad M, Jarzem P, Leroux MA, Coillard C, Chernyshov AV, Charette S, et al. Porous titanium-nickel for intervertebral fusion in a sheep model: part 1. Histomorphometric and radiological analysis. J Biomed Mater Res Appl Biomater. 2003;64B:107–20.
31. Kusakabe H, Sakamaki T, Nihei K, Oyama Y, Yanagimoto S, Ichimiya M, et al. Osseointegration of a hydroxyapatite-coated multilayered mesh stem. Biomaterials. 2004;25:2957–69. doi:10.1016/j.biomaterials.2003.09.090.
32. Bergmann G, Deuretzbacher G, Heller M, Graichen F, Rohlmann A, Strauss J, et al. Hip contact forces and gait patterns from routine activities. J Biomech. 2001;34:859–71. doi:10.1016/S0021-9290(01)00040-9.
33. Bergmann G, Graichen F, Rohlmann A. Hip joint loading during walking and running, measured in two patients. J Biomech. 1993;26:969–90. doi:10.1016/0021-9290(93)90058-M.
34. Dalstra M, Huiskes R. Load transfer across the pelvic bone. J Biomech. 1995;28:715–24. doi:10.1016/0021-9290(94)00125-N.
35. Manley MT, Ong KL, Kurtz SM. The potential for bone loss in acetabular structures following THA. Clin Orthop Relat Res. 2006;453:246–53. doi:10.1097/01.blo.0000238855.54239.fd.
36. Rydell NW. Forces acting in the femoral head-prosthesis. Acta Orthop Scand. 1966;Suppl 88:37.
37. von Eisenhart R, Adam C, Steinlechner M, Muller-Gerbl M, Eckstein F. Quantitative determination of joint incongruity and pressure distribution during simulated gait and cartilage thickness in the human hip joint. J Orthop Res. 1999;17:532–9. doi:10.1002/jor.1100170411.
38. Widmer KH, Zurfluh B, Morscher EW. Load transfer and fixation mode of press-fit acetabular sockets. J Arthroplasty. 2002;17:926–35. doi:10.1054/arth.2002.34526.
39. Dorr LD, Bloebaum R, Emmanual J, Meldrum R. Histologic, biochemical and ion analysis of tissue and fluids retrieved during total hip arthroplasty. Clin Orthop Relat Res. 1990;261:82–95.
40. Shanbhag AS, Jacobs JJ, Black J, Galante JO, Glant TT. Cellular mediators secreted by interfacial membranes obtained at revision total hip arthroplasty. J Arthroplasty. 1995;10:498–506.
41. Willert HG, Semlitsch M. Reactions of the articular capsule to wear products of artificial joint prostheses. J Biomed Mater Res. 1977;11:157–64. doi:10.1002/jbm.820110202.
42. Tolochko NK, Arshinov MK, Gusarov AV, Titov VI, Laoui T, Froyen L. Mechanisms of selective laser sintering and heat transfer in Ti powder. Rapid Prototyping J. 2003;9:314–26. doi:10.1108/13552540310502211.
43. ASTM. ASTM standard test methods of compression testing of metallic materials at room temperature. ASTM; 2000.
44. Gibson LJ, Ashby MF. Cellular solids: structure and properties. Cambridge, UK: Cambridge University Press; 1999.
45. Anselme K, Bigerelle M. Topography effects of pure titanium substrates on human osteoblast long-term adhesion. Acta Biomater. 2005;1:211–22. doi:10.1016/j.actbio.2004.11.009.
46. Mullen L, Stamp R, Brooks WK, Jones E, Sutcliffe C. Selective laser melting: a regular unit cell approach for the manufacture of porous titanium constructs suitable for orthopaedic application. J Biomed Mater Res. Part B. 2009 (in press).